GEOPHYSICS®

Sharp spatially constrained inversion of 3D FD-EMI datasets with structural prior information from GPR data: application to peat soil evaluation

Journal:	*Geophysics*
Manuscript ID	GEO-2024-0684.R2
Manuscript Type:	Technical Paper
Keywords:	electromagnetics, environmental, inversion, near surface, electrical/resistivity
Manuscript Focus Area:	Electrical and Electromagnetic Methods, Multiphysics and Joint Inversion

Sharp spatially constrained inversion of 3D FD-EMI datasets with structural prior information from GPR data: application to peat soil evaluation

Tim Klose*, **Julien Guillemoteau*** **(corresponding author julieng@uni-potsdam.de)**, **Philipp Koyan***, **Judith Walter**‡, **Giulio Vignoli**†§ **and Jens Tronicke** *

* *University of Potsdam, Institute of Geosciences, Karl-Liebknecht-Str. 24-25, 14476 Potsdam*

† *University of Cagliari, Department of Chemical and Geological Sciences, 09042 Cagliari, Italy*

‡ *State Office for Mining, Geology and Natural Resources Brandenburg (LBGR), Inselstr. 26, 03046 Cottbus, Germany*

§ *National Institute of Oceanography and Applied Geophysics (OGS), Section of Geophysics, 34010 Sgonico (TS), Italy*

(August 14, 2025)

GEO-Example

Running head: ***C-MGS inversion of FD-EMI data***

ABSTRACT

3D frequency domain electromagnetic induction (FD-EMI) surveying consists in using a profile spacing, which is smaller than the cross-line footprint of the measurements.

Using portable multi-configuration loop-loop sensors, this approach can image the spatial distribution of electrical conductivity in the shallow subsurface with a relatively high lateral resolution. A pseudo-3D sharp inversion procedure (spatially constrained 1D inversion) can be improved by using further constraints like structural prior information obtained from 3D ground-penetrating radar (GPR) surveying. Two field examples show how both structural and model sharpness constraints yield to improved pseudo-3D models compared to models as obtained from more classical approaches (e.g., non-structurally constrained and based on smoothness constraints). These results also highlight the non-uniqueness of the resulting FD-EMI conductivity models, which can critically influence the following interpretation in terms of geological units and petrophysical properties.

INTRODUCTION

FD-EMI surveying using loop-loop rigid-boom instruments is an efficient method to characterize the 3D distribution of electrical conductivity across multi-ha scale areas (De Smedt et al., 2013; Frederiksen et al., 2017; Simon et al., 2023). Typical applications include soil sciences (Doolittle and Brevik, 2014), archaeology (Tabbagh, 1986; Campana and Piro, 2008), environmental sciences (Tezkan, 1999; Pettersson and Nobes, 2003; Fitterman and Labson, 2005; Rashed and Niyazi, 2017) and civil engineering (McKenna and McKenna, 2010; Guillemoteau and Tronicke, 2015). In soil sciences, FD-EMI surveying was recently used for soil moisture characterization (Altdorff et al., 2017; Robinet et al., 2018) and monitoring (Robinson et al., 2012; Shanahan et al., 2015; Huang et al., 2017; Martini et al., 2017), soil layer imaging (von Hebel et al., 2014; Lück et al., 2022), soil salinity mapping and estimation (Khan Jadoon et al., 2015; Yao et al., 2016; Farzamian et al., 2023), and the characterization of climate-relevant peat soils (Altdorff et al., 2016; Guillemoteau et al., 2017; Beucher et al., 2020; Boaga et al., 2020; McLachlan et al., 2021b).

In soil sciences, the nonlinear 1D layered medium theory is a sufficient approximation because the typical targets (e.g., soil layers) are usually laterally extended with respect to the footprint of common rigid-boom FD-EMI instruments. Several inversion approaches and software based on the 1D approximation are thus considered to be suitable for such targets. This includes single sounding or laterally constrained inversions approaches using either smooth (Farquharson et al., 2003; von Hebel et al., 2014; Guillemoteau et al., 2016; Christiansen et al., 2016; McLachlan et al., 2021a) or sharp constraints (Deidda et al., 2020; Klose et al., 2022).

The various regularization approaches, which are used in the above-mentioned deterministic inversion methods provide different solutions. This highlights the inherent non-uniqueness of the subsurface electrical conductivity imaging problem using FD-EMI data (Klose et al., 2022). One way to evaluate and quantify this problem is to robustly determine the posterior error of the resulting 1D layered models by using probabilistic inversion. This approach is studied for the case of FD-EMI datasets in Bobe et al. (2019), Narciso et al. (2022), Liu et al. (2023), Wilken et al. (2024), and Zaru et al. (2024). In some cases, the posterior error distributions may be too large to allow for a straightforward interpretation of the results. By setting prior information from external means like boreholes data, preliminary geologic information, or complementary geophysical data (Vozoff and Jupp, 1975; Colombo and De Stefano, 2007; Moorkamp et al., 2016; Wagner and Uhlemann, 2021; Zaru et al., 2023), it is possible to reduce the ambiguity related to these large posterior errors.

The subsurface electrical conductivity models as obtained from the inversion of electric and electromagnetic data are affected by such ambiguity problem, which remains in practice a major limiting factor for a reliable geological and/or petrophysical interpretation of these models. It notably shows a trade-off between interface position and bulk properties. This effect is classically referred as T-equivalence for the case of a layered medium (Meinardus, 1970). One straightforward way to avoid the trade-off is to perform a structurally constrained inversion, i.e., to set prior information about the interface location. A basic approach consists in using a small number of model parameter whose interfaces location is fixed. In this case, one needs nevertheless an exhaustive knowledge of the interfaces in the whole investigated volume; this condition is rarely met in practice with ha-scale FD-EMI surveys. An alternative and now popular approach is to use a large number of parameters (grid-based parametrization) and to modify the topology of the model at the known location of the interface (Brown et al., 2012; Doetsch et al., 2012). This method allows to impose model sharpness where the interfaces are known, and additionally permits enough freedom for the inversion to unveil unknown interfaces. Classically, this method consists in performing a grid-based smooth inversion (Constable et al., 1987) and reducing the weight of the smoothness constraints at the interface location (Brown et al., 2012; Doetsch et al., 2012; Yan et al., 2017; Jiang et al., 2020). Klose et al. (2023) present a similar strategy to incorporate structural constraints using the focusing minimum gradient support (Portniaguine and Zhdanov, 1999) approach as background regularization (C-MGS). This method allows to promote sharp boundaries also in model regions where interfaces are not known.

In this study, we evaluate how the simultaneous inversion of a full 3D FD-EMI data set can be improved by using the C-MGS inversion method proposed in Klose et al. (2023). Here, we extend this method to the case of 3D datasets; i.e., the structural prior information is derived from a collocated 3D GPR reflection data set and is incorporated into a pseudo-3D inversion procedure with a 3D MGS regularization scheme. Firstly, we present the theory of this new structurally constrained pseudo-3D inversion procedure. Then, we apply it to two field examples, which aim at characterizing the physical and geometrical properties of peat deposits. Finally, we analyze and discuss the comparison with a standard unconstrained smooth inversion approach in view of potential subsequent petrophysical and geological interpretations.

MOTIVATION

Klose et al. (2023) have proposed the C-MGS method to include structural information as provided by GPR profiling into the 1D laterally constrained inversion (LCI, also called pseudo-2D) of loop-loop FD-EMI profiles. The C-MGS method involves incorporating an additional component, which promotes a sharp boundary at known locations of geological interfaces, into the so-called MGS operator (Portniaguine and Zhdanov, 1999). By modifying the MGS operator rather than the smoothness operator as typically done in structurally constrained grid-based inversion procedures (Brown et al., 2012; Doetsch et al., 2012; Yan et al., 2017; Jiang et al., 2020), this approach allows the promotion of sharp boundaries (and flat parameter values between boundaries) also in model regions where no interface position is known from prior information.

Portable loop-loop mono-frequency and multi-configuration FD-EMI instruments operate in the low induction number (LIN) or near-LIN domain, which by definition is characterized by a weak model dependence of the Jacobian (Guillemoteau and Tronicke, 2016), and therefore allows for a limited non-convexity of the inverse problem. Thanks to this fact, we can automatically set the starting model for an iterative deterministic minimization procedure (e.g., using a homogeneous medium equal to the mean of the observed apparent conductivity) without critically affecting the result of the inversion for interpretation, and without affecting the performance of the inversion procedure in fitting the data in practice (i.e., the minimization procedure never gets trapped in a too high local data misfit minimum). The consequence of this weak non-convexity is however visible in practice. For example, it has been highlighted in the past by comparing laterally stitched 1D models from vertically constrained inversions to pseudo-2D model resulting from 1D LCI of direct current data (Auken et al., 2005) and FD-EMI data (Klose et al., 2022). In such context, the stitched vertically constrained inversion (VCI) models are run by independent minimization processes and show some small lateral inconsistencies. On the other hand, the 1D LCI (or pseudo-2D), which by definition uses a single minimization process for an entire profile, allows to remove (although not addressing the general problem of model uncertainty/ambiguity) this modelling ”noise”.

However, the same effect appears from 2D to 3D, i.e., when stitching pseudo-2D models obtained from LCI to form a pseudo-3D model. Indeed, the inversion of an entire 3D data set implies several independent inversions (i.e., one independent inversion for every profile), which due to the weak non-convexity discussed above, show some slight inconsistencies between profiles. To illustrate this problem, we show in Figure 1 constant depth slices of the pseudo-3D model of conductivity obtained after inversion of a 3D datasets using independent C-MGS LCI (Klose et al., 2023) for each profile.

METHODOLOGY

We extend the structurally constrained minimum gradient support C-MGS LCI procedure presented in Klose et al. (2023) to the case of a pseudo-3D inversion; i.e., we aim at simultaneously inverting all the profiles of a 3D FD-EMI data set recorded across a survey area along multiple parallel profiles. For this case, the objective function to be minimized by the inversion is given by

$$\phi = [\mathbf{d} - \mathbf{f}(\mathbf{m})]^T \mathbf{W}_d [\mathbf{d} - \mathbf{f}(\mathbf{m})] + \alpha \mathbf{m}^T \mathbf{W}_m \mathbf{m}, \quad (1)$$

with

$$\mathbf{W}_m = \left[w_z \mathbf{L}_z^T \mathbf{L}_z + w_x \mathbf{L}_x^T \mathbf{L}_x + w_y \mathbf{L}_y^T \mathbf{L}_y \right], \quad (2)$$

where $\mathbf{d}$ is the data vector containing the logarithm of observed non-linear half space (NLHS) apparent conductivities, which are computed with the full non-linear homogeneous half space theory (Guillemoteau et al., 2016; Klose et al., 2022; Hanssens et al., 2019), $\mathbf{W}_d$ is a diagonal matrix of data weights inversely proportional to the square of the prior data error (Tarantola, 2005), $\mathbf{f}(\mathbf{m})$ is the vector of data computed for a given model $\mathbf{m}$ with the full non-linear layered medium theory (Wait, 1962; Ward and Hohmann, 1988), α is a Lagrange multiplier, $\mathbf{L}_{x,y,z}$ and $w_{x,y,z}$ are the C-MGS operators (Klose et al., 2023) and weights, respectively, for the three spatial directions x, y, and z. The forward modelling f of the NLHS apparent conductivity data consists of two steps (Guillemoteau et al., 2016; Klose et al., 2022). First the FD-EMI magnetic field ratios are computed in the frequency domain using (Wait, 1982; Siemon, 2001; Huang and Fraser, 2003)

$$Z^{HCP} = -s^3 \int_0^\infty r_{TE}(\lambda,\omega)\lambda^2 e^{-2\lambda h} J_0(\lambda s) d\lambda, \tag{3}$$

for the horizontal co-planar (HCP) loop-loop geometry and

$$Z^{PERPx} = s^3 \int_0^\infty r_{TE}(\lambda,\omega) e^{-2\lambda h} \lambda^2 J_1(\lambda s) d\lambda, \tag{4}$$

for the perpendicular (PERP) loop-loop geometry (Frischknecht et al., 1991). Here s is the coil distance, h is the system height above ground, J_n are Bessel functions of order n, ω is the angular frequency of the transmitter monochromatic harmonic waveform, λ is the radial component of the wave number in cylindrical coordinates. For a layered medium composed of N layers with the thickness $d_1, ..d_N$ and the conductivity $\sigma_1, ..\sigma_N$, the transverse electric (TE) reflection coefficient r_{TE} is given by (Ward and Hohmann, 1988)

$$r_{TE} = \frac{N_0 - Y_1}{N_0 + Y_1}, \quad Y_j = N_j \frac{Y_{j+1} + N_j \tanh u_j d_j}{N_j + Y_{j+1} \tanh u_j d_j}, \tag{5}$$

where $u_j = \sqrt{\lambda^2 + i\omega\mu_j\sigma_j}$, $u_0 = \lambda$, $N_j = u_j / i\omega\mu_j$ and $Y_n = N_n$. The second step of the forward modelling is to compute the robust NLHS conductivity (Guillemoteau et al., 2016) from the imaginary parts of the magnetic field ratios presented above by inverting the electrical conductivity of the equivalent homogeneous half-space. For this, we use the above formulas for the case of only one layer, although closed form formulas exists for such specific case too (Ward and Hohmann, 1988). The C-MGS operators represent non-linear spatial constraints, (i.e., it changes at every iterations), for which the smoothness is unweighted by either the spatial gradient of the model of the preceding iteration (iterative focusing process) and/or by a static 3D function $\mathbf{g}_{x,y,z}$ representing the probability of interface occurrence and reads

$$\mathbf{L}_{x,y,z}(\mathbf{m}^{(n)}) = \frac{\mathbf{D}_{x,y,z}}{\sqrt{(\mathbf{D}_{x,y,z}\mathbf{m}^{(n)})^2 + (\epsilon[\mathbf{1} + \mathbf{g}_{x,y,z}])^2}}. \tag{6}$$

Here, ϵ is commonly known as the focusing parameter of the MGS operator (Portniaguine and Zhdanov, 1999; Vignoli et al., 2021), $\mathbf{D}_{x,y,z}$ are spatial difference operators, $\mathbf{m}^{(n)}$ is the solution of the preceding iteration, and $\mathbf{g}$ is a 3D vector function, which aims to describe the probability of interface occurrence, i.e., $\mathbf{g}$ is zero where no interface is expected and values greater than zero in regions where an interface is expected or known. To design such a probability of interface occurrence, we apply the steps which are described below:

- We perform a semi-automatic interface picking within a collocated 3D block of migrated GPR constant offset data. For this, we first apply an automatic reflector detection algorithm over the entire 3D data block, and we then evaluate the outcome by a visual check for all the 2D profiles. If needed, we manually correct it.

- We compute the unit vector normal to the picked interface(s) and include it into a 3D vector field $\mathbf{n}(x, y, z)$, which is non-zero at the position of the interface(s) and zero elsewhere.

- We convolve $\mathbf{n}(x, y, z)$ with a 1D Gaussian function $\mathcal{N}(z)$ to comply with the

> propagation in depth of the GPR velocity uncertainty.
>
> $$\mathbf{g}(x,y,z) = \mathbf{0} + \mathbf{n}(x,y,z) * \mathcal{N}(z). \tag{7}$$
>
> For this aspect, we consider an error of 10% in the GPR velocity used for performing the migration. In Figure 2, we show how such an error propagates in depth along the picked reflector within an example 2D GPR section. Accordingly, the z-width of the Gaussian function increases with depth in order to account for this depth dependent GPR prior information uncertainty.

In this way, the three components of this vector function are proportional to a unit vector, which is normal to the picked interfaces (Klose et al., 2023). We minimize the objective function in equation 1 using an iterative Gauss-Newton approach known as Occam procedure (Constable et al., 1987; Aster et al., 2005) for which the following formula is computed iteratively:

$$\boldsymbol{m}^{(n+1)} = \left[\mathbf{G}^{(n)T}\mathbf{W_d}\mathbf{G}^{(n)} + \alpha_n \mathbf{W_m}\right]^{-1} \mathbf{G}^{(n)T}\mathbf{W_d}\left[\mathbf{d} + \mathbf{G}^{(n)}\boldsymbol{m}^{(n)} - \mathbf{f}(\boldsymbol{m}^{(n)})\right], \tag{8}$$

where $\mathbf{f}(\boldsymbol{m}^{(n)})$ is the forward modelling of the problem at iteration n, $\mathbf{G}$ is the Jacobian matrix, and α_n is the coefficient controlling the importance of the regularization term with respect to the data misfit. Details of the strategy for the selection of α_n as well as the stopping criteria are given in Guillemoteau et al. (2022) and mostly follows the approach discussed in Key (2016).

FIELD DATA APPLICATION

The peatland Rhinluch is located around 60 km north-west of Berlin (Figure 3). It extends around 19 km in west-east and 7 km in north-south direction and is bordered by a glacial plateau in the north. Its formation began in the end of the last glacial period (“Weichsel” ice age) during the so called “Frankfurter” and “Brandenburger” stage and is part of the “Thorn-Eberswalde” glacial valley (Kretschmer, 2000). The beginning of peat formation by processes of terrestrialisation of small post-glacial lakes and abandoned channels within the glacial valley dates back to the late glacial period around 11.000 years BP. Subsequent large-scale peat formation was caused by the extensive rise in the groundwater table because of eustatic sea level rise. This process was increased in the Middle Ages (e.g., due to deforestation, medieval mill-ponds). The Rhinluch peatland is characterized by a mean peat thickness of around 2 m, however, in former channels and depressions peat thickness can reach up to 10 m. The level of peat degradation has a significant impact on the CO_2 emission of such soil. Our ongoing research aims to assess how the imaging of the subsurface electrical conductivity using near surface geophysical methods can help to map and monitor this degradation process in order to assist decision making in the framework of local land use policy. We selected two field sites in the Rhinluch peatland region in order to evaluate the applicability of our C-MGS pseudo-3D inversion procedure. In this region, the peat layer shows a long-term degradation due to hydrological changes (mostly linked to human induced drainage since the last 200 years), which is moreover negatively influenced by artificial draining and surface ploughing for agriculture.

Both sites are located close to the localities of Kremmen and Wall, which are expected to show different states of degradation due to past drainage activities leading to decomposition and degradation of the topsoil peat. For both sites, the peat layer is underlain by a sandy environment. Following previous geophysical surveys in this region (Walter et al., 2016; Guillemoteau et al., 2017; Klose et al., 2022), the peat-sand interface is expected at a depth of a few meters and characterized by a distinct GPR reflection and a high contrast in electrical conductivity detectable by the FD-EMI method.

Acquisition

For both sites, we collected collocated 3D FD-EMI and 3D GPR data. For the FD-EMI data, we used a single frequency four-configuration DUALEM-21S sensor, which we placed at a constant height of 0.25 m above ground using a non-conductive and non-magnetic cart. The DUALEM-21S sensor simultaneously collects low induction number (LIN) apparent conductivity data (McNeill, 1980) at a rate of 10 Hz for four different loop-loop configurations: two HCP geometries with coil separation of 1 m and 2 m, and two PERP: (z-oriented transmitter magnetic dipole and x-oriented receiver magnetic coil) geometries with coil separations of 1.1 m and 2.1 m. In order to ensure that the data set is 3D (i.e., to avoid lateral aliasing), we collected the DUALEM-21S data with a sampling of ~ 0.15 m and ~ 0.5 m in the in- and crossline directions, respectively. Following Guillemoteau and Tronicke (2015), this data sampling ensures a sufficient lateral overlap of the footprints associated to the most horizontally focused channels of the DUALEM-21S sensor (PERP 1.1 m and HCP 1 m). Even though the goal of this study is to perform laterally constrained 1D layered inversion, such data density allows the identification of local 2D/3D anomalies, which can be removed by local averaging if required.

At the Kremmen site, we used non-shielded 100 MHz antennas to collect our 3D GPR data set. Similarly to the FD-EMI data (i.e., to obtain a full 3D data set with no lateral aliasing), we collected these 100 MHz GPR data with an in- and cross-line sampling of ~ 0.15 m and ~ 0.5 m, respectively. At the Wall site, we used non-shielded 200 MHz antennas. As a consequence, we reduced the cross-line sampling to ~ 0.25 m. At both sites, we also performed additional GPR common-midpoint surveys (CMP) in order to estimate the GPR propagation velocity within the peat layer.

Processing and interpretation

The standard processing sequence applied to our GPR datasets includes direct-current shift removal, zero-time correction, bandpass filtering to suppress low- and high-frequency noise and a singular value decomposition based filter (Cagnoli and Ulrych, 2001) to suppress the arrivals of the direct waves (i.e., air and ground wave). We then gridded the data to a regular grid with trace spacings of 0.2 m in inline x- and crossline y- direction. By using reflection-based spectral velocity analysis of the CMP data, we derived a peat velocity of about 0.034 m/ns in Kremmen and 0.04 m/ns in Wall. These values were subsequently used for a 3D Kirchhoff migration and time-to-depth conversion of the respective Kremmen and Wall datasets. The high amplitude reflector characterizing the peat-sand interface is then semi-automatically picked using OpendTect, a well-established seismic and GPR interpretation framework. The resulting horizon is used as structural prior information for the C-MGS inversion of FD-EMI data. The migrated GPR volume together with the picked horizon are shown in Figure 4a and 4b for both the Kremmen and the Wall field site, respectively. At both sites, the peat sand interface is detected at similar depths ($\sim 1-2$ m). However, at the Kremmen site, we observe larger lateral variations of the interface depth, indicating a quasi-circular depression, that is, a region where GPR reflections corresponding to the peat-sand-interface could not be observed anymore.

The processing of the four-configuration FD-EMI datasets includes an inline translation of the channels so that they have a common coil-coil centers, a line stripping removal using a directional spectral filter, a horizontal smoothing with a 2D gaussian filter of variance proportional to the coil separation and finally a 2D interpolation on a 0.5 m x 0.5 m grid. The resulting 3D datasets are then first inverted with the C-MGS method as introduced above using a focusing parameter of $\epsilon = 0.05$ (Klose et al., 2023). For comparison, we also inverted our data using standard smoothness constraints without any structural constraints; i.e., considering only the numerator in equation 6 (abbreviated as S in the following). In Figures 5 and 6, we show the observed NLHS apparent conductivity maps for the Kremmen and the Wall site, respectively. The shown maps indicate more lateral variability and higher conductivity at the Kremmen site. Here, we observe an area of higher conductivity indicating a circular depression of the peat-sand interface, which was already observed in our GPR results. In comparison, the NLHS conductivity maps observed in Wall (Figure 6) show less lateral variability. Note that this allows for a direct visual comparison of the four channels, which corresponds to qualitative assessment of the vertical distribution of electrical conductivity. In this respect, and looking at the channel in the order of increasing depth of investigation, the Wall NLHS apparent conductivities clearly show a three-layer medium, which is well in agreement with the expected geological setting: resistive near the surface (the degraded peat), more conductive in a second layer (non-degraded peat), and resistive again in depth (embedding sand).

Results

For the Kremmen field site, the results of the S and C-MGS inversions are shown in Figure 7. Both approaches show qualitatively similar vertical distributions of electrical conductivity, which can be characterized by three-layers. The first shallowest resistive layer is interpreted as relatively degraded peat soil layer while the second more conductive layer is non-degraded peat soils. The third rather resistive layer is the underlying sand. Note that such three layer medium could hardly be derived from a qualitative analysis of the NLHS apparent conductivity maps in Figure 5. This hence highlights the benefit of data inversion for this particular data set. For both methods, one can also observe lateral variations of electrical conductivity within the non-degraded peat layers. However, by looking at the horizontal slices in Figure 8, which cross the non-degraded peat layer, it is important to see that the S and

C-MGS methods provide significantly different results. These differences can presumably yield dissimilar petrophysical characterization of the non-degraded peat layer. The smooth model at z = -0.7 m notably shows some anomalies (black ellipses in Figure 8a), which are not visible in the C-MGS model and moreover seem to impact deeper regions of the model (see Figure 8c). The fact that both results exhibit such differences in the models while having same misfit distribution (see Figure 9) simply reveals the solution non-uniqueness. By putting more trust on the C-MGS method, which do incorporate additional information, we can interpret the lateral anomalies observed in the S result as vertical model compensations artefacts, which are typical for the S regularization. Note that in this case, we can presume that this effect is mostly controlled by the shape of the first shallow interface, as the latter lies in a model region of high data sensitivity. The horizontal slice at z = -0.7 m is located in the non-degraded (second) peat layer. The C-MGS method does not show the above-mentioned artefacts. Indeed, the C-MGS method unveils a clear circular structure centred near the point [x = 120 m,y = -30 m] and a second one, which is centred at the North-East corner of the shown slice (Figure 8b). According to information collected by push soundings and considering our GPR data, the horizontal slices at z = -1.6 m (Figure 8) are supposed to cross both the non-degraded peat layer and the sand layer. Here, the superiority of the C-MGS methods is even more clearly demonstrated as the resulting model shows more realism given the expected position of the peat-sand interface (shown as red line in Figure 8d). In contrast, the smooth model does not allows to properly detect such an interface and as discussed above, seems to be affected by artefacts, which are controlled by the morphology of the upper part of the model. Lastly, this unintended vertical cumulation of information reproduces the typical drawback, associated with the interpretation of non-inverted apparent conductivity (by definition, such apparent conductivities represent the information integrated over a column of subsurface). That being said, and one more time in view of a petrophysical translation of the resulting electrical conductivity model, it is fair to admit that the effort of performing a sophisticated and time-consuming inversion using such an approach could be questioned and more data-driven approaches could be favoured in practice.

However, here by using structural prior constraints combined with the MGS regularization, whose premise is to provide more realistic models, we demonstrate with the C-MGS method that the inversion of the FD-EMI data can fulfil its essential role in geophysical imaging: to unveil features that are not visible in the data in a straightforward manner.

We performed the same procedure with the data acquired in Wall. Similarly to the Kremmen case, both S-and C-MGS methods exhibit the same data misfit distribution (see Figure 9). As insinuated for the Kremmen case, this is a particularly desired condition to fairly compare different inversion results and for the present study, to identify and objectively analyse the non-uniqueness of the solution. We show the results of the S and C-MGS inversions in Figure 10 . Here, we can see that this site can also be characterized by three layers, which are interpreted from top to bottom as degraded peat, non-degraded peat and sand. As predictable from the poor lateral variations shown in the NLHS apparent conductivity maps (Figure

6), the lateral variations of both interfaces and layer electrical conductivities are smaller than for the Kremmen case. The horizontal slice z = -0.6 m, which lies within the conductive non-degraded peat layer (Figure 11a and 11b) shows some lateral variations of electrical conductivity. We observe nevertheless that these lateral variations are significantly attenuated by the C-MGS method. This result shows that in practice, the interpretation of the C-MGS model implies a more homogeneous non-degraded peat layer than the interpretation of the smooth model. By assuming again that the C-MGS method is the most robust thanks to the incorporation of additional information, we can claim that it reduces noise in the peat layer electrical conductivity, which is probably caused by imaging artefact. Similarly to the Kremmen case, the black ellipses in Figure 11a and 11c represents model compensation artefact which may bias the interpretation of model slices. The horizontal slices at z = -1.35 m (Figure 11c and 11d) crosses both sand and non-degraded peat layer and shows indeed that the C-MGS method better delineates the peat-sand interface as well as a more laterally homogeneous sand layer.

Peat soils typically show a porosity larger than 85% (Hobbs, 1986). Accordingly, its electrical conductivity is mostly driven by the porous space. It follows that dry peat layers are particularly resistive as observed in the top 30 cm at both Kremmen and Wall sites ($\sim$ 5 mS/m). If saturated with water, the peat layer is relatively conductive as observed below 30 cm, also at both Kremmen and Wall sites ($\sim$ 50 mS/m). Here, it is important to specify that for both sites, the water table at the time of the survey was below 2 m, i.e., within the sand layer underlying the peat layer. This means that the saturation of the peat layer can be attributed to water retention capabilities, which is a proven gauge for assessing peat soil integrity (Schnitzer, 1986). Another criterion to assess the state of peat is the ionic concentration of the pore-space fluid as the degraded peat releases more sulphates into the pore-space water (Casagrande, 1987). Although further borehole samples analysis is needed to better understand the contribution of each process to the electrical conductivity of the peat layer, our results show that our new structurally constrained approach suggests less lateral variability in peat degradation than the standard unconstrained smooth inversion approach for both Kremmen and Wall FD-EMI datasets.

CONCLUSION

When 3D FD-EMI datasets collected with portable multi-configuration sensor are inverted, the reconstructed 3D subsurface electrical conductivity model may be subject to petrophysical conversion and/or geometrical analysis of particular 2D planes (e.g., horizontal or vertical slices). In this study, we inverted two 3D FD-EMI field datasets using rather standard smooth regularization and using the recently proposed C-MGS method, which we have here purposely extended in 3D. With these two field examples, we highlight that an unconstrained smooth inversion can yield critical bias in the petrophysical and geometrical interpretation of the result, mostly due to structure/bulk properties ambiguity, but also due to model compensation artefacts, which are hard to read in 3D. The proposed C-MGS methods corrects these two effects and we demonstrate in this study that the resulting models can yield rather different interpretations. As a consequence, it appears that the direct interpretation of smooth inversion of FD-EMI data alone should be taken cautiously, especially for a petrophysical conversion of the results. If the collection of relevant structural information is feasible, it should be encouraged to allow for the proposed C-MGS inversion or similar. As demonstrated in the present study, such an approach may significantly improve the robustness of the resulting electrical conductivity model and, as a matter of fact, its subsequent petrophysical and geological interpretation.

ACKNOWLEDGMENTS

This project has been funded by the Deutsche Forschungsgemeinschaft (DFG; grant number 418056756). We thank Andreas Herrmann who supported us for the planning of the field campaigns by taking contact with the landlords. We also thank Marko Dubnitzki, Stella Grace Nzouatchoua Tchana and Luisa Heinig who helped us to collect the field datasets.

REFERENCES

Altdorff, D., M. Bechtold, J. Van der Kruk, H. Vereecken, and J. Huisman, 2016, Mapping peat layer properties with multi-coil offset electromagnetic induction and laser scanning elevation data: Geoderma, **261**, 178–189.

Altdorff, D., C. von Hebel, N. Borchard, J. van der Kruk, H. R. Bogena, H. Vereecken, and J. A. Huisman, 2017, Potential of catchment-wide soil water content prediction using electromagnetic induction in a forest ecosystem: Environmental earth sciences, **76**, 1–11.

Aster, R., B. Borchers, and C. Thurber, 2005, Parameter Estimation and Inverse Problems: Elsevier Academic Press.

Auken, E., A. V. Christiansen, B. H. Jacobsen, N. Foged, and K. I. Sorensen, 2005, Piecewise 1D laterally constrained inversion of resistivity data: Geophysical Prospecting, **53**, 497–506.

Beucher, A., T. Koganti, B. V. Iversen, and M. H. Greve, 2020, Mapping of Peat Thickness Using a Multi-Receiver Electromagnetic Induction Instrument: Remote Sensing, **12**, 2458.

Boaga, J., A. Viezzoli, G. Cassiani, G. Deidda, L. Tosi, and S. Silvestri, 2020, Resolving the thickness of peat deposits with contact-less electromagnetic methods: A case study in the venice coastland: Science of The Total Environment, **737**, 139361.

Bobe, C., E. Van De Vijver, J. Keller, D. Hanssens, M. Van Meirvenne, and P. De Smedt, 2019, Probabilistic 1-d inversion of frequency-domain electromagnetic data using a kalman ensemble generator: IEEE Transactions on Geoscience and Remote Sensing, **58**, 3287–3297.

Brown, V., K. Key, and S. Singh, 2012, Seismically regularized controlled-source electromagnetic inversion: Geophysics, **77**, no. 1, E57–E65.

Cagnoli, B., and T. Ulrych, 2001, Singular value decomposition and wavy reflections in ground-penetrating radar images of base surge deposits: Journal of applied geophysics, **48**, 175–182.

Campana, S., and S. Piro, 2008, Seeing the unseen. geophysics and landscape archaeology: CRC press.

Casagrande, D., 1987, Sulphur in peat and coal: Geological Society, London, Special Publications, **32**, 87–105.

Christiansen, A. V., J. B. Pedersen, E. Auken, N. E. Søe, M. K. Holst, and S. M. Kristiansen, 2016, Improved geoarchaeological mapping with electromagnetic induction instruments from dedicated processing and inversion: Remote Sensing, **8**, 1022.

Colombo, D., and M. De Stefano, 2007, Geophysical modeling via simultaneous joint inversion of seismic, gravity, and electromagnetic data: Application to prestack depth imaging: The Leading Edge, **26**, 326–331.

Constable, S. C., R. L. Parker, and C. G. Constable, 1987, Occams inversion: a practical algorithm for generating smooth models from electromagnetic sounding data: Geophysics, **52**, 289–300.

De Smedt, P., T. Saey, A. Lehouck, B. Stichelbaut, E. Meerschman, M. Monirul Islam, E. Van de Vijver, and M. Van Meirvenne, 2013, ”Exploring the potential of multi-receiver EMI survey for geoarchaeological prospection: A 90 ha dataset: Geoderma, **199**, 30–36.

Deidda, G. P., P. D. de Alba, G. Rodriguez, and G. Vignoli, 2020, Inversion of multiconfiguration complex EMI data with minimum gradient support regularization: A case study: Mathematical Geosciences, 1–26.

Doetsch, J., N. Linde, M. Pessognelli, A. G. Green, and T. Günther, 2012, Constraining 3-d electrical resistance tomography with gpr reflection data for improved aquifer characterization: Journal of Applied Geophysics, **78**, 68–76.

Doolittle, J. A., and E. C. Brevik, 2014, The use of electromagnetic induction techniques in soils studies: Geoderma, **223**, 33–45.

Farquharson, C., D. Oldenburg, and P. Routh, 2003, Simultaneous 1D inversion of loop-loop electromagnetic data for magnetic susceptibility and electrical conductivity: Geophysics, **68**, 1857–1869.

Farzamian, M., F. Bouksila, A. M. Paz, F. M. Santos, N. Zemni, F. Slama, A. B. Slimane, T. Selim, and J. Triantafilis, 2023, Landscape-scale mapping of soil salinity with multi-height electromagnetic induction and quasi-3d inversion in saharan oasis, tunisia: Agricultural Water Management, **284**, 108330.

Fitterman, D. V., and V. F. Labson, 2005, Electromagnetic induction methods for environmental problems: 301–356.

Frederiksen, R. R., A. V. Christiansen, S. Christensen, and K. R. Rasmussen, 2017, A direct comparison of EMI data and borehole data on a 1000 ha data set: Geoderma, **303**, 188–195.

Frischknecht, F., V. Labor, B. Spies, and W. Anderson, 1991, Profiling methods using small sources: in Nabighian, M.N., Electromagnetic methods in applied geophysics, volume 2.

Guillemoteau, J., N. B. Christensen, B. H. Jacobsen, and J. Tronicke, 2017, Fast 3D multi-channel deconvolution of electromagnetic induction loop-loop apparent conductivity data sets acquired at low induction numbers: Geophysics, **82**, no. 6, E357–E369.

Guillemoteau, J., P. Sailhac, C. Boulanger, and J. Trules, 2015, Inversion of ground constant offset loop-loop electromagnetic data for a large range of induction numbers: Geophysics, **80**, no. 1, E11–E21.

Guillemoteau, J., F. Simon, E. Lück, and J. Tronicke, 2016, 1D sequential inversion of portable multi-configuration electromagnetic induction data: Near Surface Geophysics, **14**, 411–420.

Guillemoteau, J., and J. Tronicke, 2015, Non-standard ground conductivity meter configurations: evaluating sensitivities and applicability: Journal of Applied Geophysics, **118**, 15–23.

———, 2016, Evaluation of a rapid hybrid spectral-spatial domain 3D forward modeling approach for loop-loop electromagnetic induction quadrature data acquired in low-induction-number environments: Geophysics, **81**, no. 6, E447–E458.

Guillemoteau, J., G. Vignoli, J. Barreto, and G. Sauvin, 2022, Sparse laterally constrained inversion of surface-wave dispersion curves via minimum gradient support regularization: Geophysics, **87**, no. 3, R281–R289.

Hanssens, D., S. Delefortrie, C. Bobe, T. Hermans, and P. De Smedt, 2019, Improving the reliability of soil ec-mapping: Robust apparent electrical conductivity (reca) estimation in ground-based frequency domain electromagnetics: Geoderma, **337**, 1155–1163.

Hobbs, N., 1986, Mire morphology and the properties and behaviour of some british and foreign peats: Quarterly Journal of Engineering Geology, **19**, 7–80.

Huang, H., and D. Fraser, 2003, Inversion of helicopter electromagnetic data to a magnetic conductive layered earth: Geophysics, **68**, 1211–1223.

Huang, J., E. Scudiero, W. Clary, D. Corwin, and J. Triantafilis, 2017, Time-lapse monitoring of soil water content using electromagnetic conductivity imaging: Soil use and management, **33**, 191–204.

Jiang, C., J. Igel, R. Dlugosch, M. Müller-Petke, T. Günther, J. Helms, J. Lang, and J. Winsemann, 2020, Magnetic resonance tomography constrained by ground-penetrating radar for improved hydrogeophysical characterization: Geophysics, **85**, no. 6, JM13–JM26.

Key, K., 2016, Mare2dem: a 2-d inversion code for controlled-source electromagnetic and magnetotelluric data: Geophysical Journal International, **207**, 571–588.

Khan Jadoon, Z., D. Moghadas, A. Jadoon, T. Missimer, S. Al-Mashharawi, and M. McCabe, 2015, Estimation of soil salinity in a drip irrigation system by using joint inversion of multicoil electromagnetic induction measurements: Water Resources Research, **51**, 3490–3504.

Klose, T., J. Guillemoteau, G. Vignoli, and J. Tronicke, 2022, Laterally constrained inversion (lci) of multi-configuration emi data with tunable sharpness: Journal of Applied Geophysics, **196**, 104519.

Klose, T., J. Guillemoteau, G. Vignoli, J. Walter, A. Herrmann, and J. Tronicke, 2023, Structurally constrained inversion by means of a minimum gradient support regularizer: examples of fd-emi data inversion constrained by gpr reflection data: Geophysical Journal International, **233**, 1938–1949.

Kretschmer, H., 2000, Einführung - naturräumliche einordnung des untersuchungsgebietes , in: Ökologisches entwicklungskonzept oberes rhinluch: Zalf Bericht, 4–7.

Liu, M., J. Narciso, D. Grana, E. Van De Vijver, and L. Azevedo, 2023, Frequency-domain electromagnetic induction for the prediction of electrical conductivity and magnetic susceptibility using geostatistical inversion and randomized tensor decomposition: Geophysics, **88**, no. 6, E159–E171.

Lück, E., J. Guillemoteau, J. Tronicke, J. Klose, and B. Trost, 2022, Geophysical sensors for mapping soil layers–a comparative case study using different electrical and electromagnetic sensors, *in* Information and communication technologies for agriculture—theme I: sensors: Springer, 267–287.

Martini, E., U. Werban, S. Zacharias, M. Pohle, P. Dietrich, and U. Wollschläger, 2017, Repeated electromagnetic induction measurements for mapping soil moisture at the field scale: Validation with data from a wireless soil moisture monitoring network: Hydrology and Earth System Sciences, **21**, 495–513.

McKenna, S. P., and J. R. McKenna, 2010, Modeling and analysis of the response of a triaxial, frequency-domain electromagnetic induction sensor to a buried linear conductor: Geophysics, **75**, no. 1, F1–F14.

McLachlan, P., G. Blanchy, and A. Binley, 2021a, Emagpy: Open-source standalone software for processing, forward modeling and inversion of electromagnetic induction data: Computers & Geosciences, **146**, 104561.

McLachlan, P., G. Blanchy, J. Chambers, J. Sorensen, S. Uhlemann, P. Wilkinson, and A. Binley, 2021b, The application of electromagnetic induction methods to reveal the hydrogeological structure of a riparian wetland: Water Resources Research, **57**, e2020WR029221.

McNeill, J., 1980, Electromagnetic terrain conductivity measurements at low induction numbers: Technical Note TN-6, Geonics Ltd.

Meinardus, H. A., 1970, Numerical interpretation of resistivity soundings over horizontal beds: Geophysical Prospecting, **18**, 415–433.

Moorkamp, M., P. G. Lelièvre, N. Linde, and A. Khan, 2016, Integrated imaging of the earth: Theory and applications: John Wiley & Sons, **218**.

Narciso, J., C. Bobe, L. Azevedo, and E. Van De Vijver, 2022, A comparison between kalman ensemble generator and geostatistical frequency-domain electromagnetic inversion: The impacts on near-surface characterization: Geophysics, **87**, no. 5, E335–E346.

Pettersson, J. K., and D. C. Nobes, 2003, Environmental geophysics at scott base: ground penetrating radar and electromagnetic induction as tools for mapping contaminated ground at antarctic research bases: Cold regions science and technology, **37**, 187–195.

Portniaguine, O., and M. S. Zhdanov, 1999, Focusing geophysical inversion images: Geophysics, **64**, 874–887.

Rashed, M., and B. Niyazi, 2017, Environmental impact assessment of the former almusk lake wastewater dumpsite using electromagnetic induction technique: Earth Systems and Environment, **1**, 1–10.

Robinet, J., C. von Hebel, G. Govers, J. van der Kruk, J. P. Minella, A. Schlesner, Y. Ameijeiras-Mariño, and J. Vanderborght, 2018, Spatial variability of soil water content and soil electrical conductivity across scales derived from electromagnetic induction and time domain reflectometry: Geoderma, **314**, 160–174.

Robinson, D. A., H. Abdu, I. Lebron, and S. B. Jones, 2012, Imaging of hill-slope soil moisture wetting patterns in a semi-arid oak savanna catchment using time-lapse electromagnetic induction: Journal of Hydrology, **416**, 39–49.

Schnitzer, M., 1986, Water retention by humic substances.

Shanahan, P. W., A. Binley, W. R. Whalley, and C. W. Watts, 2015, The use of electromagnetic induction to monitor changes in soil moisture profiles beneath different wheat genotypes: Soil Science Society of America Journal, **79**, 459–466.

Siemon, B., 2001, Improved and new resistivity-depth profiles for helicopter electromagnetic data: Journal of Applied Geophysics, **46**, 65–76.

Simon, F.-X., B. Fores, G. Hulin, L. Deschodt, and J. Guillemoteau, 2023, 3dmcd/1dlci inversion of an fd-emi dataset: the case study of the paleolandscape of bourbourg/loon-plage (france): Advances in On-and Offshore Archaeological Prospection: Proceedings of the 15th International Conference on Archaeological Prospection, 435–438.

Tabbagh, A., 1986, Applications and advantages of the Slingram electromagnetic method for archaeological prospecting: Geophysics, **51**, 576–584.

Tarantola, A., 2005, Inverse Problem Theory: Society for Industrial and Applied Mathematics, Philadelphia.

Tezkan, B., 1999, A review of environmental applications of quasi-stationary electromagnetic techniques: Surveys in Geophysics, **20**, 279–308.

Vignoli, G., J. Guillemoteau, J. Barreto, and M. Rossi, 2021, Reconstruction, with tunable sparsity levels, of shear wave velocity profiles from surface wave data: Geophysical Journal International, **225**, 1935–1951.

von Hebel, C., S. Rudolph, A. Mester, J. Huisman, P. Kumbhar, H. Vereecken, and J. van der Kruk, 2014, Three-dimensional imaging of subsurface structural patterns using quantitative large-scale multiconfiguration electromagnetic induction data: Water Resources Research, **50**, 2732–2748.

Vozoff, K., and D. Jupp, 1975, Joint inversion of geophysical data: Geophysical Journal International, **42**, 977–991.

Wagner, F. M., and S. Uhlemann, 2021, An overview of multimethod imaging approaches in environmental geophysics: Advances in Geophysics, **62**, 1–72.

Wait, J., 1982, Geo-electromagnetism: Academic Press Inc.

Wait, J. R., 1962, A note on the electromagnetic response of a stratified earth: Geophysics, **27**, 382–385.

Walter, J., G. Hamann, E. Lück, C. Klingenfuss, and J. Zeitz, 2016, Stratigraphy and soil properties of fens: Geophysical case studies from northeastern germany: Catena, **142**, 112–125.

Ward, S. H., and G. W. Hohmann, 1988, Electromagnetic theory for geophysical applications: Electromagnetic methods in applied geophysics—theory, Society of Exploration Geophysicists, 131–311.

Wilken, D., M. Mercker, P. Fischer, A. Vott, E. Erkul, E. Corradini, and N. Pickartz, 2024, Artificial bee colony algorithm with adaptive parameter space dimension: A promising tool for geophysical electromagnetic induction inversion: Remote Sensing, **16**, 470.

Yan, P., T. Kalscheuer, P. Hedin, and M. A. Garcia Juanatey, 2017, Two-dimensional magnetotelluric inversion using reflection seismic data as constraints and application in the COSC project: Geophysical Research Letters, **44**, 3554–3563.

Yao, R., J. Yang, D. Wu, W. Xie, P. Gao, and W. Jin, 2016, Digital mapping of soil salinity and crop yield across a coastal agricultural landscape using repeated electromagnetic induction (emi) surveys: PloS one, **11**, e0153377.

Zaru, N., M. Rossi, G. Vacca, and G. Vignoli, 2023, Spreading of localized information across an entire 3d electrical resistivity volume via constrained emi inversion based on a realistic prior distribution: Remote Sensing, **15**, 3993.

Zaru, N., S. Silvestri, M. Assiri, P. Bai, T. Hansen, and G. Vignoli, 2024, Probabilistic petrophysical reconstruction of danta's alpine peatland via electromagnetic induction data: ESSOAR, **47**, 251–259.

CAPTIONS

Figure 1: Example of a pseudo-3D model made by stitching pseudo-2D models obtained with the C-MGS LCI method presented in Klose et al. (2023). The lines/profiles are oriented toward x-direction. a) Depth slice at z = -0.3 m and b) Depth slice at z = -1.35 m. The depth slices highlight the inconsistency of the models in the cross-line direction.

Figure 2: Example of 3D vector function **g** describing the probability of interface oc-

currence shown for one selected profile for the sake of simplicity. a) Interface picked from a 3D GPR data set. b),c) and d),vertical, inline and cross-line component of **g** showing a gaussian function centred on the interface position and with variance increasing with depth in agreement with the depth-dependant error caused by the GPR velocity uncertainty (here, fixed to 10%).

Figure 3: Location of the two field sites near the localities of Wall and Kremmen, Brandenburg, Germany.

Figure 4: Processed and interpreted 3D GPR data set for a) the Kremmen site and b) the Wall site. The coloured surface is a horizon interpreted from picked GPR reflections, which we interpret as the peat-sand interface.

Figure 5: Kremmen field site: FD-EMI data set after processing and conversion into NLHS apparent conductivity σ_a^{NLHS} . Increasing depth of investigation channel order: PERP1.1m, PERP2.1m, HCP1m, HCP2m. The white rectangle corresponds to an area where data affected by the presence of a permanent metallic box have been muted.

Figure 6: Wall field site: FD-EMI data set after processing and conversion into NLHS apparent conductivity σ_a^{NLHS} (Guillemoteau et al., 2015, 2016; Hanssens et al., 2019) . The channels are displayed from top to bottom following an increasing depth of investigation.

Figure 7: Pseudo-3D models of electrical conductivity obtained after inversion of the FD-EMI data collected at the Kremmen site using a) the S method and b) the C-MGS method. The red lines indicate the picked horizon from the GPR imaging result (Figure 4a), which we interpret as the peat-sand interface.

Figure 8: Depth slices of the resulting pseudo-3D models obtained with the S and C-MGS methods for the Kremmen data set. a) S model and b) C-MGS model at z = -0.7 m. c) S model and d) C-MGS model at z = -1.6 m. The red lines indicate the position of the reflector picked from the GPR imaging result. The black ellipses in the smooth model indicate areas where shallow features seem to impact the solution also in the deep slice. The reversal of the sign of these anomalies is a typical compensation near a large contrast, which is often observed with smooth regularization.

Figure 9: Data misfits generated by the S and C-MGS methods for a),b) the Kremmen and c),d) the Wall datasets in term of relative error of the NLHS apparent conductivity. The mean global misfits is provided in the graphic title for each case. For the Kremmen case, data fitting slightly under-performs (although remains below 5%) because of a systematic error for one channel (HCP1m) observed between $y = 10$ m and $y = 25$ m. This error has a low absolute value at the order of the noise level (i.e., < 1 mS/m). Here, we see nevertheless that both inversion approaches handle this error in a similar manner by providing almost exactly the same misfit distribution, which is a critical criteria to study and validate the non-uniqueness of the solution.

Figure 10: Pseudo-3D models of electrical conductivity obtained after inversion of the FD-EMI data collected in the Wall site using a) the S method and b) the C-MGS method. The red lines indicate the picked horizon from the GPR imaging result (Figure 4b), which we interpret as the peat-sand interface.

Figure 11: Depth slices of the resulting pseudo-3D models obtained with the S and C-MGS methods for the Wall data set. a) and b) respectively S and C-MGS models at z = -0.6 m. b) and c) respectively S an C-MGS models at z = -1.35 m. The

red lines indicate the position of the reflector picked from the GPR imaging result. The black circles in the smooth model indicate areas where shallow features seem to impact the solution also in the deep slice.

LIST OF FIGURES

6 Wall field site: FD-EMI data set after processing and conversion into NLHS apparent conductivity σ_a^{NLHS} (Guillemoteau et al., 2015, 2016; Hanssens et al., 2019) . The channels are displayed from top to bottom following an increasing depth of investigation.

7 Pseudo-3D models of electrical conductivity obtained after inversion of the FD-EMI data collected at the Kremmen site using a) the S method and b) the C-MGS method. The red lines indicate the picked horizon from the GPR imaging result (Figure 4a), which we interpret as the peat-sand interface.

8 Depth slices of the resulting pseudo-3D models obtained with the S and C-MGS methods for the Kremmen data set. a) S model and b) C-MGS model at z = -0.7 m. c) S model and d) C-MGS model at z = -1.6 m. The red lines indicate the position of the reflector picked from the GPR imaging result. The black ellipses in the smooth model indicate areas where shallow features seem to impact the solution also in the deep slice. The reversal of the sign of these anomalies is a typical compensation near a large contrast, which is often observed with smooth regularization.

9 Data misfits generated by the S and C-MGS methods for a),b) the Kremmen and c),d) the Wall datasets in term of relative error of the NLHS apparent conductivity. The mean global misfits is provided in the graphic title for each case. For the Kremmen case, data fitting slightly under-performs (although remains below 5%) because of a systematic error for one channel (HCP1m) observed between $y = 10$ m and $y = 25$ m. This error has a low absolute value at the order of the noise level (i.e., < 1 mS/m). Here, we see nevertheless that both inversion approaches handle this error in a similar manner by providing almost exactly the same misfit distribution,

which is a critical criteria to study and validate the non-uniqueness of the solution.

10 Pseudo-3D models of electrical conductivity obtained after inversion of the FD-EMI data collected in the Wall site using a) the S method and b) the C-MGS method. The red lines indicate the picked horizon from the GPR imaging result (Figure 4b), which we interpret as the peat-sand interface.

11 Depth slices of the resulting pseudo-3D models obtained with the S and C-MGS methods for the Wall data set. a) and b) respectively S and C-MGS models at z = -0.6 m. b) and c) respectively S an C-MGS models at z = -1.35 m. The red lines indicate the position of the reflector picked from the GPR imaging result. The black circles in the smooth model indicate areas where shallow features seem to impact the solution also in the deep slice.

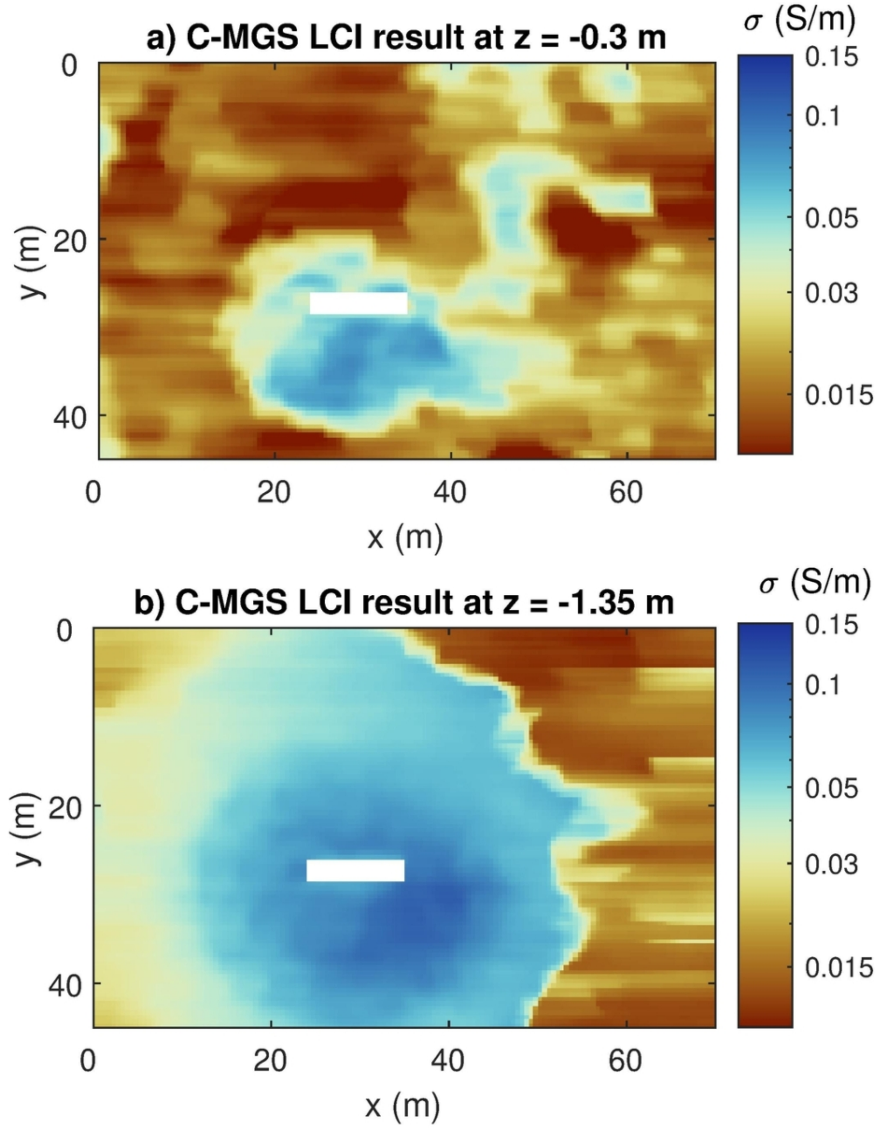

Figure 1. Example of a pseudo-3D model made by stitching pseudo-2D models obtained with the C-MGS LCI method presented in Klose *et al* (2023). The lines/profiles are oriented toward x-direction. a) Depth slice at z = -0.3 m and b) Depth slice at z = -1.35 m. The depth slices highlight the inconsistency of the models in the cross-line direction.

97x123mm (300 x 300 DPI)

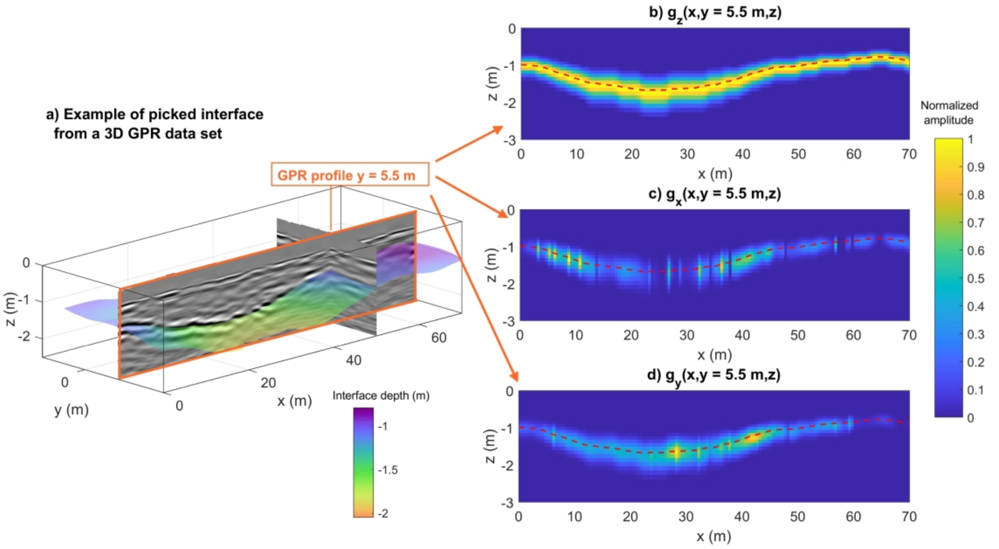

Figure 2. Example of 3D vector function **g** describing the probability of interface occurrence shown for one selected profile for the sake of simplicity. a) Interface picked from a 3D GPR data set. b),c) and d),vertical, inline and cross-line component of **g** showing a gaussian function centred on the interface position and with variance increasing with depth in agreement with the depth-dependant error caused by the GPR velocity uncertainty (here, fixed to 10%).

307x185mm (300 x 300 DPI)

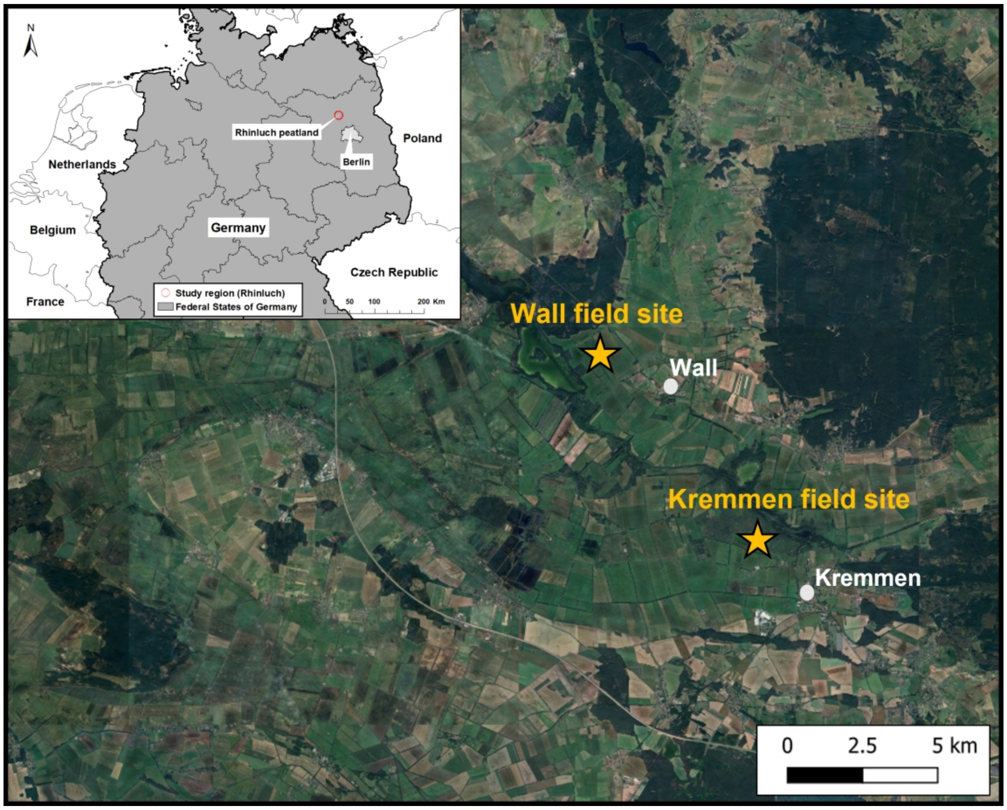

Figure 3. Location of the two field sites near the localities of Wall and Kremmen, Brandenburg, Germany.

461x370mm (130 x 130 DPI)

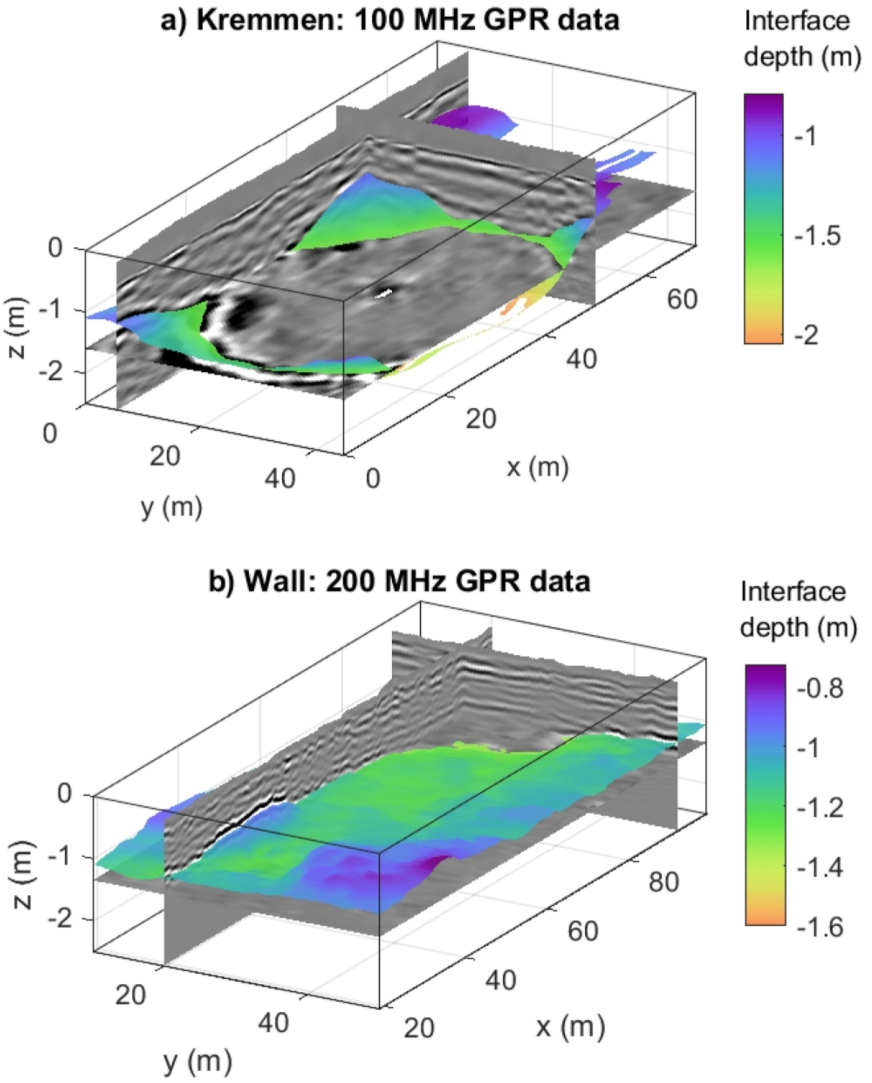

Figure 4. Processed and interpreted 3D GPR data set for a) the Kremmen site and b) the Wall site. The coloured surface is a horizon interpreted from picked GPR reflections, which we interpret as the peat-sand interface.

114x153mm (300 x 300 DPI)

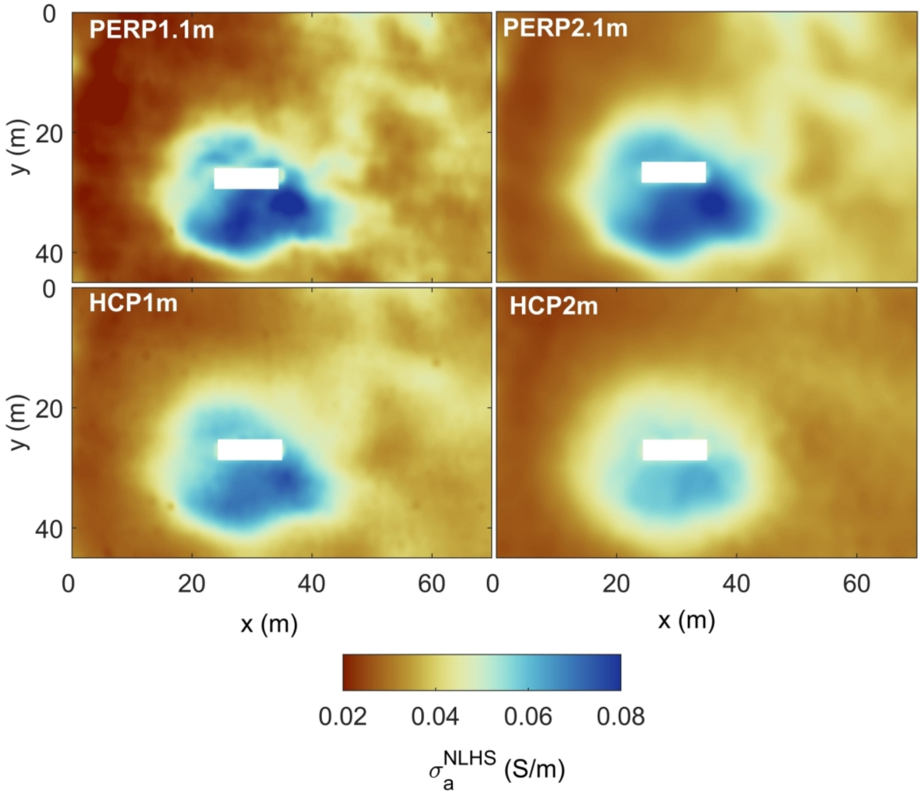

Figure 5. Kremmen field site: FD-EMI data set after processing and conversion into NLHS apparent conductivity $\sigma_a{}^{NLHS}$. Increasing depth of investigation channel order: PERP1.1m, PERP2.1m, HCP1m, HCP2m. The white rectangle corresponds to an area where data affected by the presence of a permanent metallic box have been muted.

196x166mm (300 x 300 DPI)

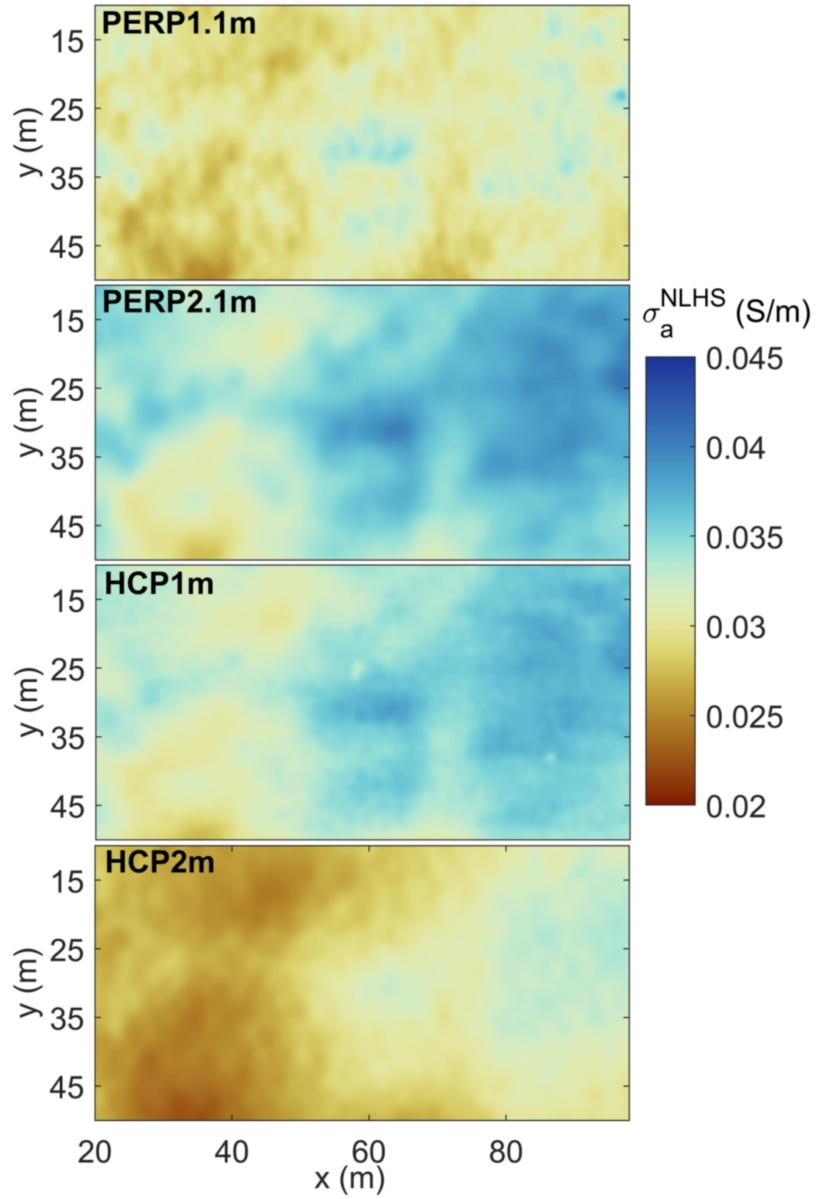

Figure 6. Wall field site: FD-EMI data set after processing and conversion into NLHS apparent conductivity $\sigma_a{}^{NLHS}$ (Guillemoteau *et al.*, 2015, 2016; Hanssens *et al.*, 2019). The channels are displayed from top to bottom following an increasing depth of investigation.

141x190mm (300 x 300 DPI)

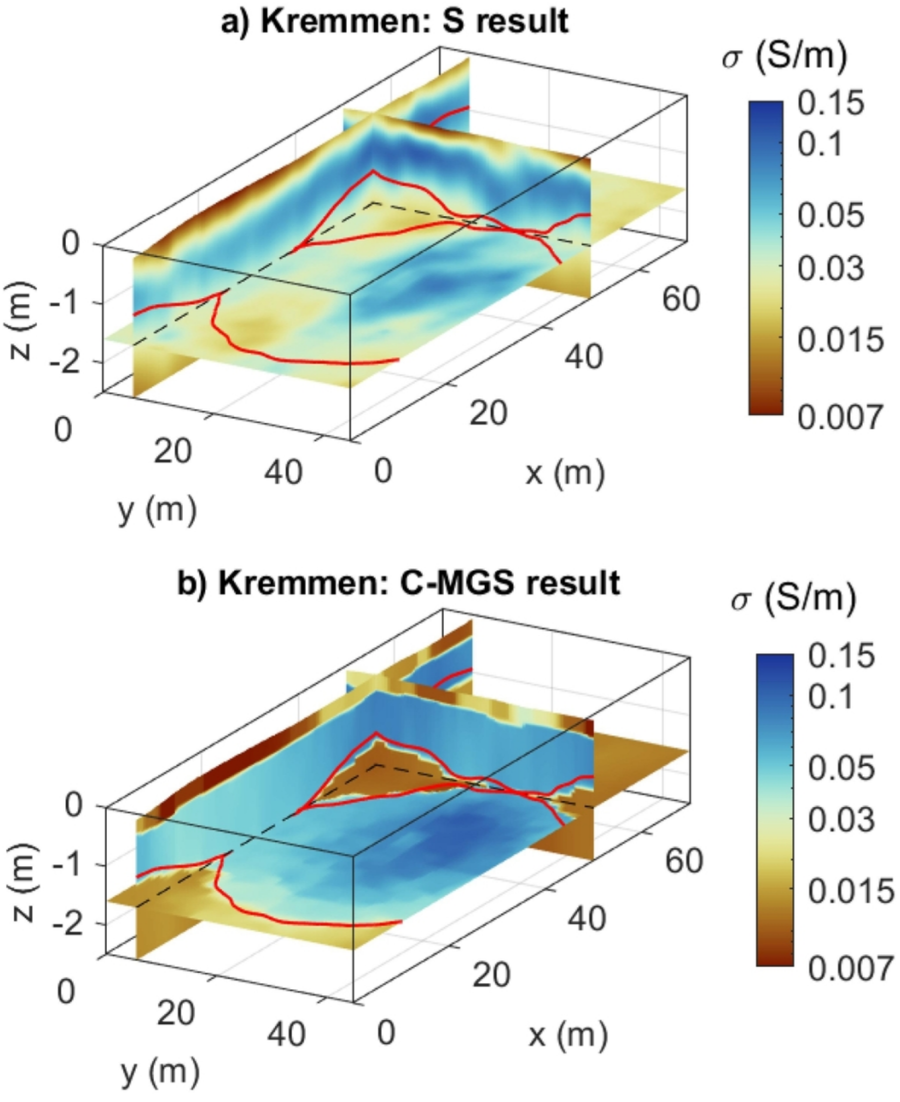

Figure 7. Pseudo-3D models of electrical conductivity obtained after inversion of the FD-EMI data collected at the Kremmen site using a) the S method and b) the C-MGS method. The red lines indicate the picked horizon from the GPR imaging result (Figure 4a), which we interpret as the peat-sand interface.

104x133mm (300 x 300 DPI)

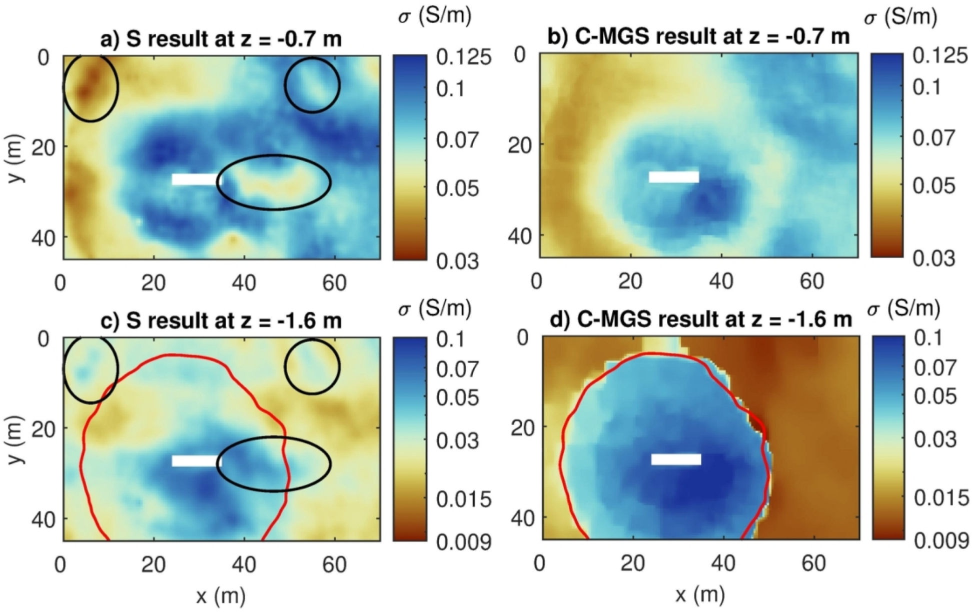

Figure 8. Depth slices of the resulting pseudo-3D models obtained with the S and C-MGS methods for the Kremmen data set. a) S model and b) C-MGS model at z = -0.7 m. c) S model and d) C-MGS model at z = -1.6 m. The red lines indicate the position of the reflector picked from the GPR imaging result. The black ellipses in the smooth model indicate areas where shallow features seem to impact the solution also in the deep slice. The reversal of the sign of these anomalies is a typical compensation near a large contrast, which is often observed with smooth regularization.

141x94mm (300 x 300 DPI)

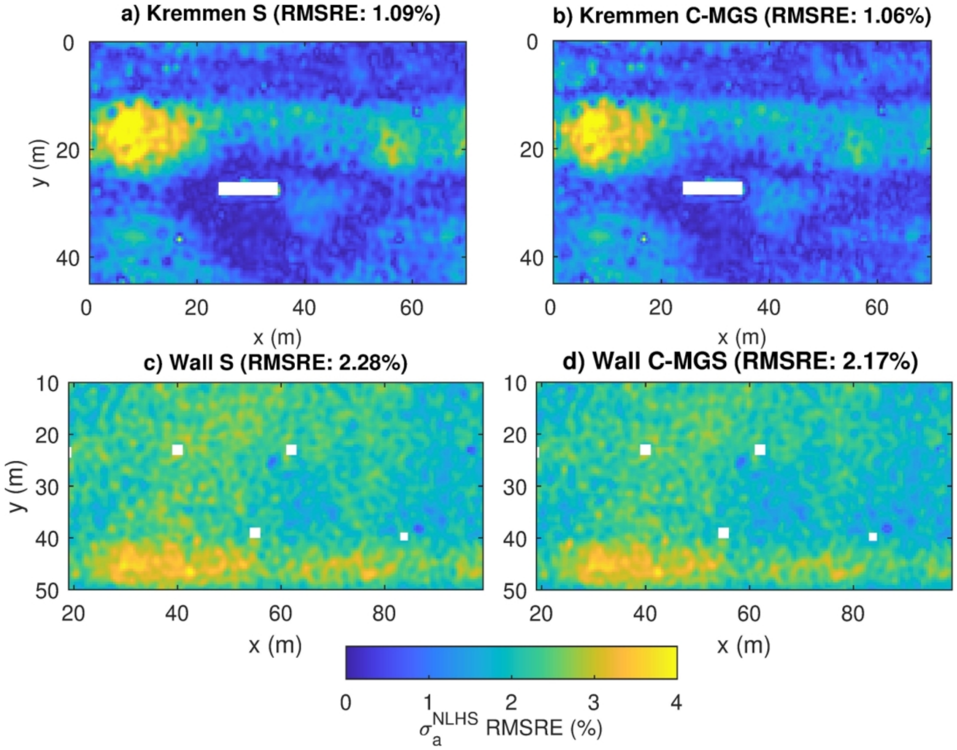

Figure 9. Data misfits generated by the S and C-MGS methods for a),b) the Kremmen and c),d) the Wall datasets in term of relative error of the NLHS apparent conductivity. The mean global misfits is provided in the graphic title for each case. For the Kremmen case, data fitting slightly under-performs (although remains below 5\%) because of a systematic error for one channel (HCP1m) observed between y = 10 m and y = 25 m. This error has a low absolute value at the order of the noise level (i.e., < 1 mS/m). Here, we see nevertheless that both inversion approaches handle this error in a similar manner by providing almost exactly the same misfit distribution, which is a critical criteria to study and validate the non-uniqueness of the solution.

162x124mm (300 x 300 DPI)

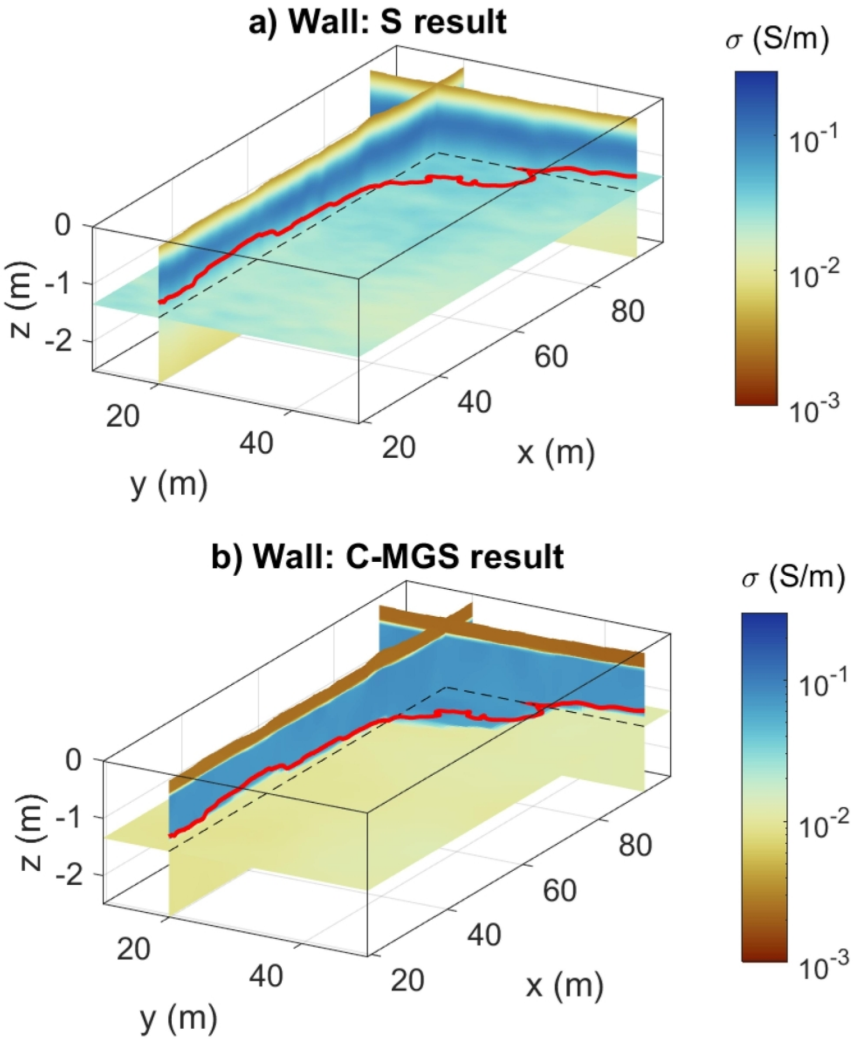

Figure 10. Pseudo-3D models of electrical conductivity obtained after inversion of the FD-EMI data collected in the Wall site using a) the S method and b) the C-MGS method. The red lines indicate the picked horizon from the GPR imaging result (Figure 4b), which we interpret as the peat-sand interface.

145x188mm (300 x 300 DPI)

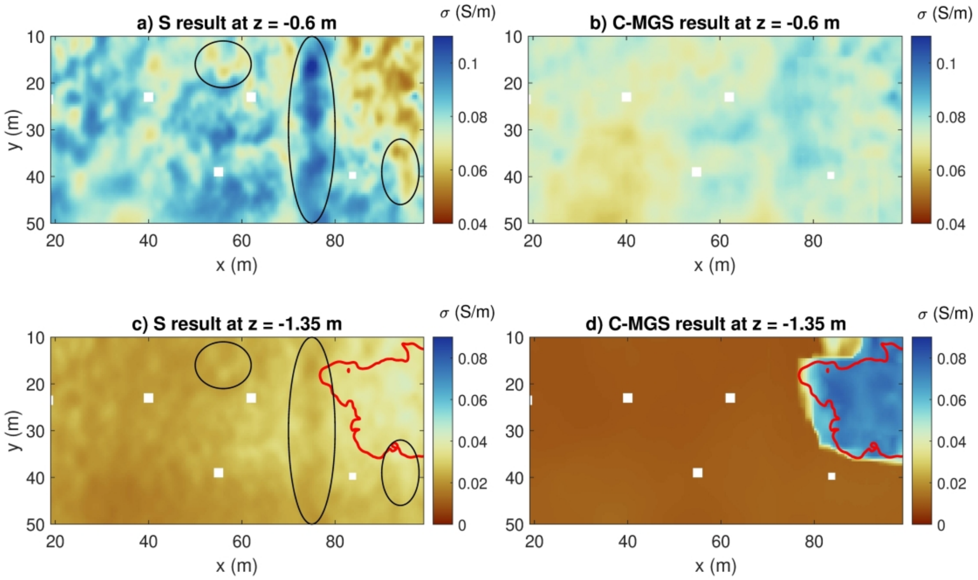

Figure 11. Depth slices of the resulting pseudo-3D models obtained with the S and C-MGS methods for the Wall data set. a) and b) respectively S and C-MGS models at *z* = -0.6 m. b) and c) respectively S an C-MGS models at *z* = -1.35 m. The red lines indicate the position of the reflector picked from the GPR imaging result. The black circles in the smooth model indicate areas where shallow features seem to impact the solution also in the deep slice.

292x217mm (300 x 300 DPI)

DATA AND MATERIALS AVAILABILITY

Data associated with this research are available and can be obtained by#xD;#xA;contacting the corresponding author.

DOI:10.1190/geo2024-0684.1